Monitoring Failure Sequence in Cold-sprayed Al6061 Deposits Using Acoustic Emission

Zi Wen THAM,[a] *Santhakumar SAMPATH,*[a] *Yi Fan CHEN,*[a] *Augustine CHEONG Kok Heng,*[a] *Li Tian CHEW,*[a] *Debbie SENG Hwee Leng,*[a] *Pei WANG,*[a] *Shijie WANG,*[a] *Zheng ZHANG,*[a#] *Lei ZHANG*[a*]

[a] Institute of Materials Research and Engineering (IMRE), Agency for Science, Technology and Research (A*STAR), 2 Fusionopolis Way, Innovis #08-03, Singapore 138634, Republic of Singapore

Corresponding Authors:

[*] E-mail address: zhangl@imre.a-star.edu.sg

[#] E-mail address: zhangz@imre.a-star.edu.sg

ABSTRACT

Cold spray (CS) is a recent addition to the thermal spray family with extensive research conducted on the effects of different process parameters during CS deposition various metallic powders. While mechanical and fatigue strengths of cold-sprayed deposits have been evaluated through static and dynamic testing, identifying the sequence of failure mechanisms - whether cracks within the coating occur before delamination at the coating-substrate interface - remains visually challenging but crucial for pinpointing weak points within the deposit. To address this, acoustic emission (AE) testing was employed in this study to reliably determine the failure sequence through *in-situ* monitoring. Using a four-point bending setup, a 2.5 mm thick Al6061 coating on an Al6061-T6 substrate was analyzed in real-time with AE data and video correlation. The findings revealed that cracks associated with higher AE frequencies (≥ 100 kHz) appeared first, accompanied subsequently by delamination, which was correlated with lower frequencies AE events (< 100 kHz). This AE methodology shows promise for integration with other static tests, such as open-hole tension as well as fatigue testing to determine similar failure sequences. By providing a clear understanding of failure mechanisms, this approach advances the structural evaluation of cold-sprayed deposits and their potential applications.

Keywords: Acoustic Emission; Cold Spray; Al6061; Crack; Delamination; Non-destructive Test

I. Introduction

Cold spray (CS) is a new member in the family of thermal spray techniques. It mainly uses the kinetic energy of metallic particles with or without low thermal energy to create metallic coatings and deposits typically on metallic substrates [1-3]. Due to its low process temperature (≤ 1000 ^{o}C), powder oxidation and phase transformation can be largely avoided during CS deposition. This technique has been developed to repair, modify and fabricate a variety of metallic components using both single-element metal powders (i.e, copper (Cu), aluminium (Al), nickel (Ni), commercial pure titanium (Ti), silver (Ag), zinc (Zn), chromium (Cr)) and alloy powders (such as Al alloys [4,5], Ti-6Al-4V [6,7], stainless steel [8], nickel-based alloy [9,10] and CoNiCrAlY powders [1,11], etc) in aerospace [12-14], automotive [14], marine and offshore [15] and other manufacturing industries. CS is an ideal technique to deposit heat-sensitive powders (i.e., Al alloys, Ti alloys, bulk metallic glass, etc) with minimum powder oxidation, and it is also used to repair heat-sensitive substrates (i.e., magnesium alloys) and substrates considered un-weldable by welding techniques (i.e., Al7075, Al2024) due to their rapid loss of strength at temperatures as low as 150°C [16].

There have been extensive investigations about the influence of various key process parameters (including gas pressure, gas temperature, standoff distance, traverse speed, etc) on the microstructure, deposition efficiency and static adhesion strength of CS deposits [11]. In recent years, considerable efforts have been focused on fatigue performance of CS deposits. Examples include fatigue strength evaluation of a hole in Al357-T6 cast alloy repaired using Al357 powders [17], fastener holes in Al2024-T351 and Al7075-T651 plates repaired using respective powders [18], groove in Al2024-T3 plate to simulate aircraft skin [19] and a crack represented by a 30° V-notch in Al2099 plate [12], etc. Most of these investigations were conducted post-mortem through examining the fractured or broken surfaces after the static and fatigue failure, as well as postulating the crack development pathway and failure sequence. It is highly desired if the failure mechanisms and failure sequence of CS deposits under both static and fatigue loading can be probed *in-situ* with direct evidence. Such knowledge would help identify the weak point in the CS deposits. Subsequently, surface treatment and process parameters optimization can be fine-tuned to improve the weak regions' strength specifically. In this paper, acoustic emission (AE) testing was proposed as the *in-situ* testing method to address this need.

AE testing is a non-invasive and passive non-destructive testing (NDT) technique that detects acoustic emissions, which are transient elastic stress waves generated when materials subjected to stress loading undergo permanent microstructural changes (such as crack initiation, propagation, frictional movement, deformation, impact, etc) [20-22]. Signals from AE spectra including peak amplitude, duration, frequency, counts, rise time, decay time, frequency spectra and polarity signal parameters are very useful for characterization [23,24]. AE testing has been applied widely in various industries, including aerospace [25,26], civil engineering [23,27], mechanical engineering [28] and materials science [29], due to its ability to monitor structural integrity and materials' health in real-time without disrupting their normal operation. In cold spray, AE has been deployed to monitor and differentiate between particle impacts and defective events (such as delamination and internal cracking) during 90Ta-10W powders' deposition on steel substrate [30]. Inline process monitoring using AE sensors have also been reported during air plasma spray deposition of titanium powders [21].

The growing use of cold spray in the repair and manufacturing of metallic components necessitates a thorough investigation about the failure sequence during mechanical testing, which is crucial for assessing the structural integrity and reliability of cold-sprayed deposits. In this study, we employ AE testing to investigate the failure sequence during four-point bending of cold-sprayed Al6061 deposits. Al6061 is of technological importance due to its widespread industrial applications and desirable mechanical properties. It would be crucial to assess the failure sequence of cold-sprayed Al6061 deposits in actual deployment scenarios, i.e., whether internal crack or interfacial delamination take place first during loading. AE analysis can provide real-time information about the initiation, growth, and evolution of cracks and delamination in the deposited material non-destructively. In this study, the four-point bending test is selected instead of three-point bending, as it offers simple yet versatile method for evaluating the flexural properties and fracture behavior of materials. In three-point bending tests, the maximum shear stress is concentrated below the central loading pin, where the cracks can be controlled to initiate and propagate intentionally. This test is particularly suitable for homogeneous materials, as only the central material experiences the maximum shear stress. Conversely, in four-point bending tests, the maximum bending stress is uniformly distributed over a larger specimen between the inner two support pins. This approach is particularly useful for evaluating non-homogeneous materials, such as composites, where difference in composition or internal defects could lead to deviation in results. The larger sampling region can lead to a more representative result of the entire sample. Furthermore, four-point bending is useful for brittle materials which cannot withstand shear stresses effectively. Given that cold-sprayed Al6061 deposit is brittle and non-homogeneous due to random distribution of pores, the four-point bending serves as an ideal test setup for the present sample.

To investigate the behavior of cold-sprayed Al6061 deposits, three geometries will be evaluated: samples without a precut, samples with a 1 mm precut, and samples with a 3 mm radius groove. By correlating AE signals with the stress-strain response of the deposits, we aim to elucidate the failure sequence of cold-sprayed Al6061 deposits under bending loads, which is challenging to identify visually. The test protocol of combining AE with four-point bending test can be similarly applied to deposits prepared by other thermal spray techniques (like atmospheric plasma spray, flame spray, high velocity oxyfuel spray, etc) and other test setups (i.e., three-point bending, open hole tension, even fatigue test, etc).

II. Experimental methods

The Al6061 powders (SAAM-AL6061-G1H1-2) used in this paper were procured from Solvus Global. Particle size distribution was analysed using a Malvern Mastersizer 2000 particle size analyser, while the powders' morphology and chemical composition were analysed with JEOL JSM-7600F field emission scanning electron microscopy (FE-SEM). The Al6061 powders were sprayed using Centerline SST EPX high pressure cold spray system onto an Al6061-T6 plate (300 mm wide × 400 mm long × 12 mm thick), which was brushed using a wire wheel followed by an alcohol wipe prior to deposition. The Al6061 powders were pre-heated at 280°C by nitrogen (N_2) carrier gas and fed into the spray gun where N_2 was also used as the propellant gas. The standoff distance between the spray gun and the substrate was 15 mm. The powders were then deposited at a N_2 pressure of 3.5 MPa and temperature of 500°C. The first layer was deposited with the spray gun set at 30° to the surface plane, and the subsequent layer was deposited when the spray gun was set at 90° to the substrate. The 30° spray effectively eliminated the surface native oxide, exposing a fresh aluminum surface that enhances deposition efficiency when spaying at 90°. A total of 3.2 mm thick Al6061 was deposited onto the substrate. Thereafter, six samples with a dimension of 200.0 mm length × 20.0 mm width × 8.5 mm thickness were cut via wire electrical discharge machining (EDM). The details of the six samples were further described in the Results section.

The four-point bending tests were conducted using an Instron 5900R universal mechanical tester with a 50 kN load cell. The supporting and loading pins' diameters were 5.0 mm, and the supporting and loading spans were 40 and 80 mm, respectively. Two types of AE sensors including Mistra WD sensor and the Mistra F15a sensor were used for detecting the AE events. The former sensor has a wide bandwidth of 125 to 1000 kHz, peak sensitivity of -62 dB and is also a differential sensor, which uses two sensing elements polarised in opposite directions. This reduces common mode noises resulting in high signal-to-noise ratio (SNR).

The latter sensor has a narrower bandwidth of 100 to 450 kHz and higher sensitivity at -61 dB. Each sensor was connected to a pre-amplifier that boosts the collected AE signals by a gain of 60 dB. The two sensors were mounted at the edge of the coupons using a spring clamp, equidistant away from the midspan and coupled with ultrasonic gel couplant. The AE signals were collected by the SAEU3H multi-channel AE data acquisition system and processed with the native SWAE software from QingCheng Ltd. The data acquisition system was configured with a 3 MHz sampling rate and 10k sample length, and the other AE parameters were set with the following: 40 dB threshold, 300 μs peak definition time (PDT), 600 μs hit definition time (HDT) and 1000 μs hit-locking time (HLT). The detection threshold was calibrated just above the ambient noise amplitude of the bending setup. A 12MP RGB camera from Daheng Imaging was configured with a field-of-view (FOV) of 62 × 45 mm and used to record the video during the four-point bending tests, which were carried out until the 2.5 mm Al6061 deposits were cracked and delaminated visibly from the substrates below the crack point. The fractured surfaces were analysed under the same JEOL JSM-7600F SEM.

III. Results

The SEM image in Fig. 1(a) shows that the Al6061 powders were dominated with spherical shapes. Powder size analysis shows that D_{10}, D_{50} and D_{90} of the Al6061 powders were 23.3, 34.4 and 51.0 μm, respectively (Fig. 1(b)). After the cold spray deposition, the original flat and smooth Al6061-T6 plate shown in Fig. 1(c) was covered with a rough but continuous 3.2 mm thick Al6061 deposit (Fig. 1(d)), which adhered tightly to the underlying substrate without delamination. The cross-sectional microstructure seen at the top right corner of Fig. 1(d) shows that the interface is very intimate without visible cracks at the interface, although alternative peak and trough were observed along the spray direction due to overlapping of neighboring spray paths. Despite the considerable 3.2 mm thickness, no wrapping of the deposit nor the substrate plate was observed along the four edges of the plate.

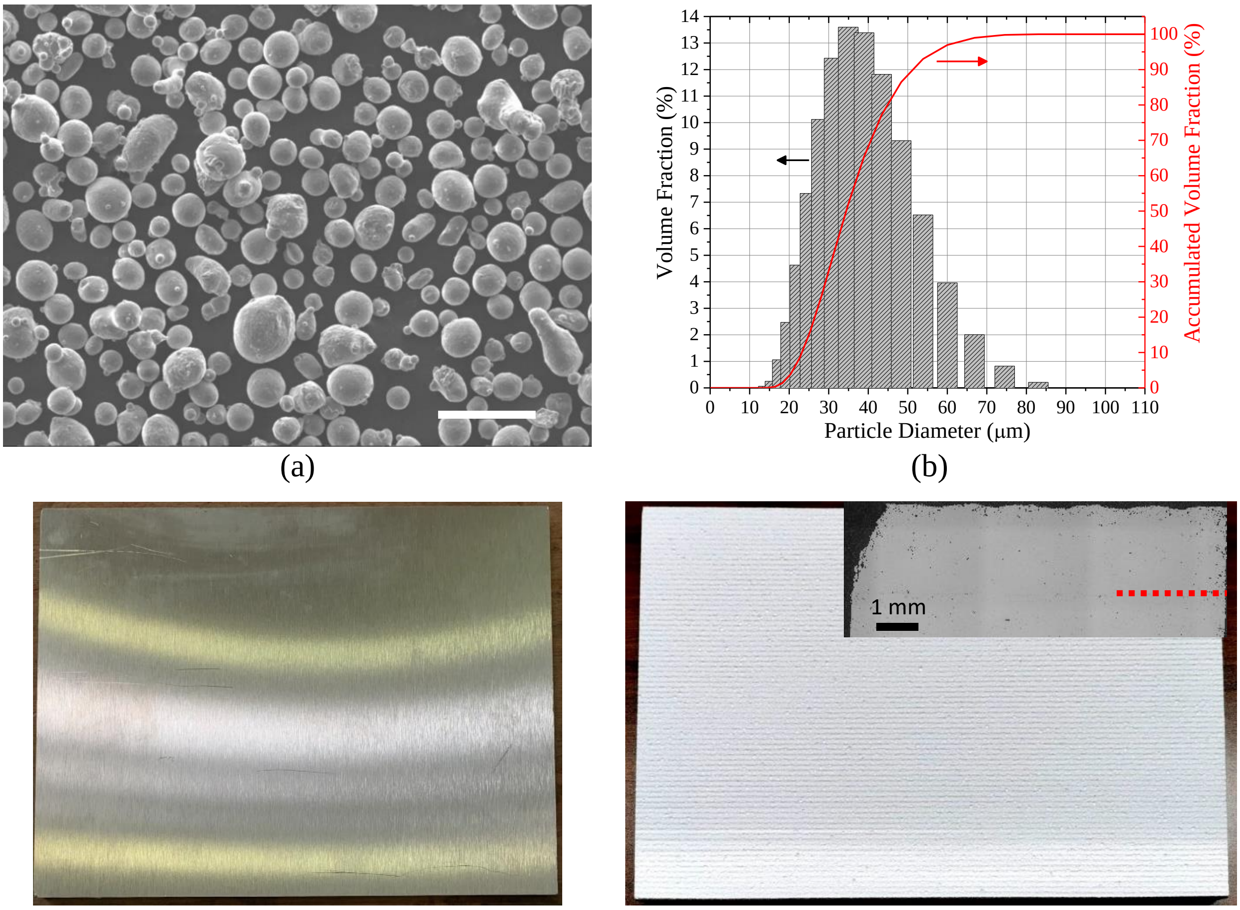

Fig.1 (a) SEM image of the as-received Al6061 powders (scale bar representing 100 μm), (b) Al6061 powder size distribution, (c) as-received 30 cm wide × 40 cm long × 12 mm thick Al6061-T6 plate and (d) the same plate after 3.2 mm thick Al6061 coating deposition. The inset at the top right corner of the (d) shows the cross-sectional image of 2.5 mm coating (after cutting away the surface undulation with electrical discharge machining). The red dotted line indicates the interface between Al6061 deposit and the Al6061-T6 substrate.

To eliminate the surface roughness caused by the overlapping of spray paths, wire electrical discharge machining (EDM) was used to remove 0.5 mm from the top surface of the deposit. This process produced a smooth and uniform deposit of 2.5 mm, ensuring an adequate thickness for monitoring crack development, given that the wire used in EDM has a diameter of 0.2 mm. Subsequently, a 5.8 mm thick Al6061-T6 substrate was cut away from the backside of the original 12 mm thick substrate. This resulted in a remaining 6 mm substrate in order to withstand the residual stress from the 2.5 mm Al6061 deposit without bending. The overall thickness also considered the limitation of the maximum load capacity (50 kN) of Instron

5900R universal mechanical tester. Although a thinner deposit, ranging from 1.0 to 2.0 mm, is sufficient to determine the sequence of failure occurrence, the 2.5 mm deposit is necessary to assess the fatigue performance of the cold-sprayed Al6061 deposits in a separate study. Moreover, thicker deposit provides a longer duration for each stage of damage evolution, aiding in AE behavior analysis. Two of such as-prepared coupons are shown in Fig. 2(a).

In addition, two coupons were machined to have a 1.0 mm deep pre-cut at the centre of the coating (Fig. 2(b)) and another two coupons were machined to have a 1.0 mm deep groove with radius of 3 mm (R3, Fig. 2(c)). The pre-cut and groove at the centre ensure that the centre of the coupon has the thinnest thickness (t) so that the nominal flexural stress ($\sigma_{f,nominal}$) at the centre was maximum under the same loading force (F) based on the Equation 1,

$$\sigma_{f,nominal} = \frac{3}{4}\frac{F \times L}{w \times t^2} \quad (1)$$

where F is the loading force in Newton, L is the support span in mm, w is width of test beam in mm and t is depth or thickness of tested beam in mm. At a loading force of 1000 N, the nominal flexural stress between inner two loading pins is 41.5 MPa for the sample without precut after considering L, w and t to be 80 mm, 20 mm and 8.5 mm respectively. For the samples with 1 mm precut and groove sample, the nominal flexural stress increased to 53.3 MPa as t reduced to 7.5 mm. The presence of precut and groove introduces stress concentration factor (K_t, usually > 1) below the precut and groove, which increases the maximum stress ($\sigma_{f,max}$) under the precut and groove substantially based on Equation (2):

$$K_t = \frac{\sigma_{f,max}}{\sigma_{f,nominal}} \quad (2)$$

Hence, cracks can thus be ensured to take place below the precut or groove for reliable video monitoring. The groove configuration provides a more gradual and continuous material profile around the thinnest centre region than the 1mm precut configuration. The actual four-point bending setup in the Instron 5900R can be seen in Fig. 2(d), where the Mistra WD wideband and the Mistra F15a sensor were mounted at the top of the deposit and clamped on the left and right of the coupon, respectively.

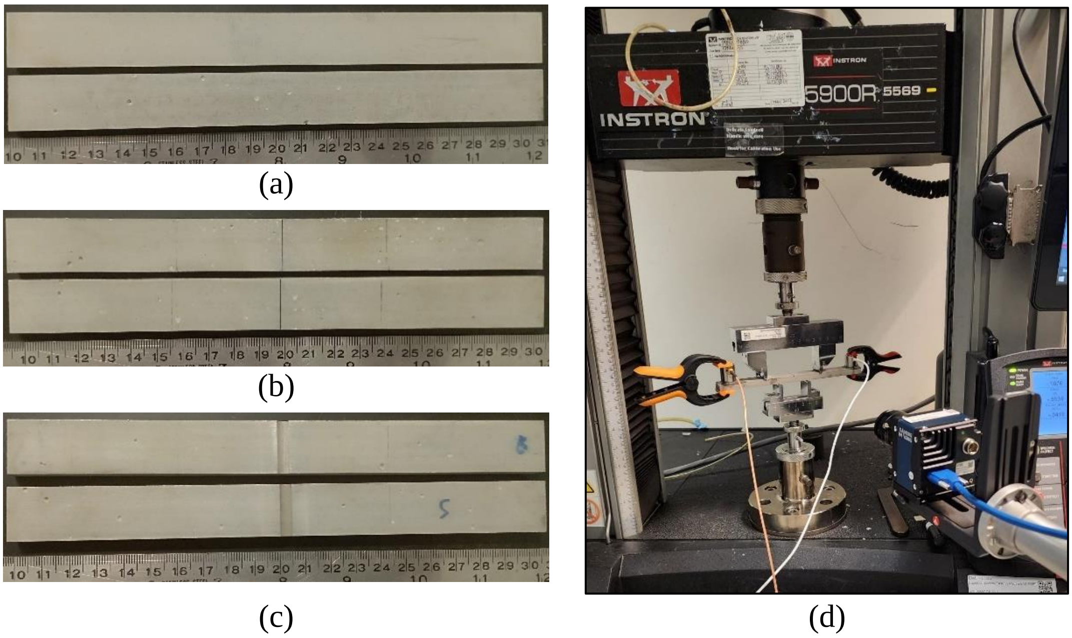

Fig.2 Three sets of coupons for four-point bending test after wire electrical discharge machining: (a) two as-prepared 2.5 mm Al6061 deposit on 6.0 mm Al6061-T6 coupons, (b) two coupons with 1 mm precut at the center of the Al6061 deposit, (c) two coupons with R3 groove and 1 mm depth at the center and (d) actual setup of a four-point bending test with two acoustic sensors clicked at two ends during the four-point bending test.

After conducting the four-point bending test on the precut sample, the crack can be clearly observed below the precut notch, and the delamination between the deposit and the interface is also visible. The cross-sectional micrograph of the tested sample with 1mm precut is presented in Fig. 3(a). Additionally, SEM analysis of the delaminated Al6061 deposit exhibits the presence of flattened powder particles (Fig. 3(b)). In contrast, the Al6061-T6 substrate surface is predominantly decorated with craters, with occasional Al6061 particles remaining (Fig. 3(c)). The SEM images clearly reveal that the delamination took place between the cold-sprayed Al6061 deposits and the Al6061-T6 coupon.

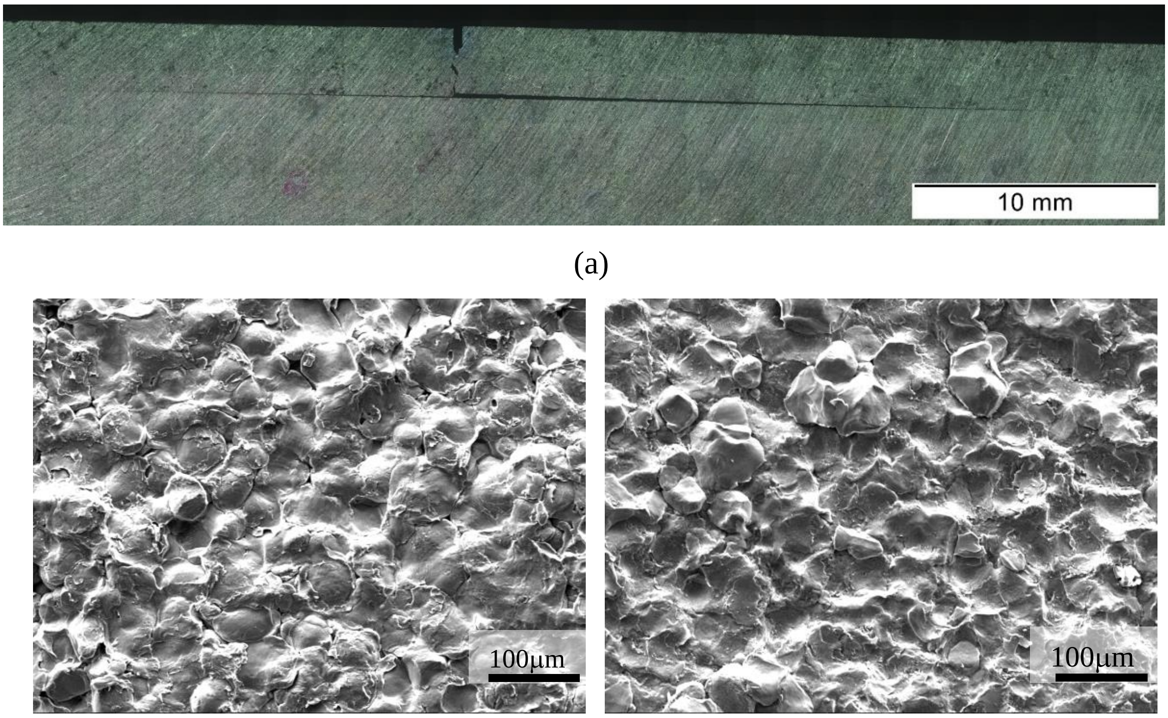

(b) (c)

Fig 3. (a) Cross-sectional micrograph of the 1mm precut sample after four-point bending test and SEM image from the delaminated interface showing (b) cold sprayed deposit with presence of flattened Al6061 powder particles and (c) Al6061-T6 substrate surface decorated dominantly with craters bombarded by Al6061 powder particles.

A typical AE acquisition during a four-point bending test of a coupon with a pre-cut (Fig. 2(b)) is shown in Fig. 4(a), overlapped with the loading-time curve extracted from the Instron 5900R at 0.5 mm/s loading rate. Each scattered red square and blue dots represent an individual acoustic emission (AE) event detected by the Mistra WD or F15a sensors, respectively. The first AE emission event was detected at 21.7 s at a load of 1178.4 N, 2.2 s ahead of the yielding point at 23.9 s and 1246.7 N (marked by green downward arrow in Fig. 4(a)). After yielding, there was a sharp drop in loading force within 0.9 s to 1198.6 N till 24.8 s, followed by a plateau in loading force which remained stable at 1198 N till 37.7 s. Subsequently the loading force continued to increase linearly with time. The corresponding video can be found in the Supplementary Information.

From 76.6 s onwards, the captured video shows that the entire deposit cracked completely from the tip of precut downwards and reached the interface with the substrate. Only delamination between the CS deposit and the substrate continued to propagate from the center towards the inner two pins (Fig. 4(g)). The gap between deposit and substrate increased concurrently with the outward delamination growth. The corresponding frequencies of the acoustic emissions were in the low frequency range (< 100 kHz) for both F15a (~ 51.0 kHZ, blue curve) and WD sensors (dominated with ≤ 200 kHz, red curve, Fig. 4(f)) and had a duration of 1120 µs. Typically, high frequency and lower frequency AE events are associated with small scale and larger scale failure events, respectively [31]. For example, delamination along the deposit/substrate interface typically would involve a much larger area of failure when compared to cracks within the deposits. A correlation of a delamination event to the low frequency components seen in the FFT spectrum can also be confirmed by the captured image (Fig. 4(g)), where the delamination of the deposit and substrate dominates all other failure mechanisms. Similar frequency characteristics have been reported in plasma sprayed thermal barrier coatings, where the AE signature of cracks and delamination were 100 to 300 kHz and <100 kHz, respectively [32,33].

On the contrary, at the first detected acoustic emission events at 21.7 s (Fig. 4(b)), the real time image (Fig. 4(c)) showed no indications of either crack or delamination on the external surface, even after zooming in the image. The high frequency components within 200 to 300 kHz were captured by both sensors (Fig. 4(b)). This AE event had a duration 183 µs and was likely to be emitted from cracking within the deposit, starting from regions where the adhesion was weak. At this point of time, the first crack has yet to propagate to the external surface and hence was not visible under the camera.

In short, when comparing the acoustic emission events at 21.7 s and 76.6 s (Fig. 4(f)), a clear distinction emerges between these two types of AE events. The high frequency components at 21.7 s correlates with a cracking failure mechanism and the low frequency components at 76.6 s are shown to be related to delamination. Other two discrete frequencies at 32.4 and 117.0 kHz detected by both sensors are likely to attributed to the noise during the loading.

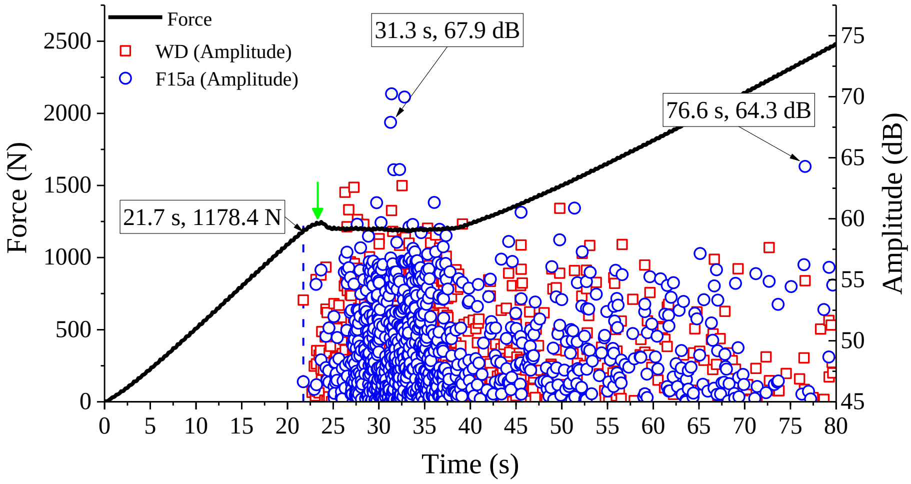
Force
WD (Amplitude)
F15a (Amplitude)
31.3 s, 67.9 dB
76.6 s, 64.3 dB
21.7 s, 1178.4 N
Force (N)
Amplitude (dB)
Time (s)

(a)

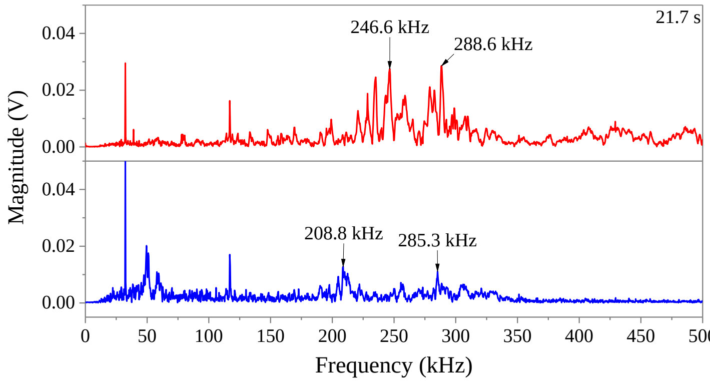
21.7 s
246.6 kHz
288.6 kHz
208.8 kHz
285.3 kHz
Magnitude (V)
Frequency (kHz)

(b)

(c)

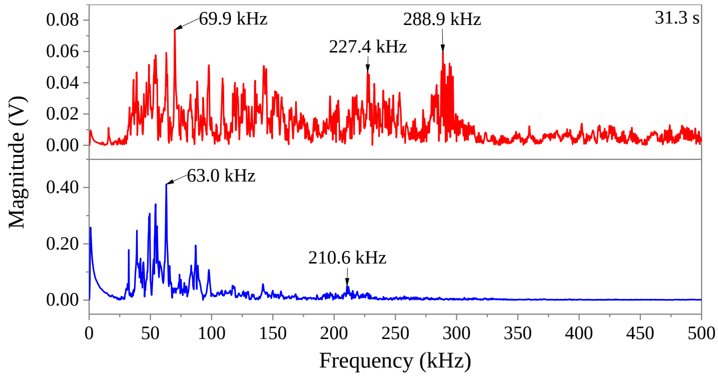
31.3 s
69.9 kHz
288.9 kHz
227.4 kHz
63.0 kHz
210.6 kHz
Magnitude (V)
Frequency (kHz)

(d)

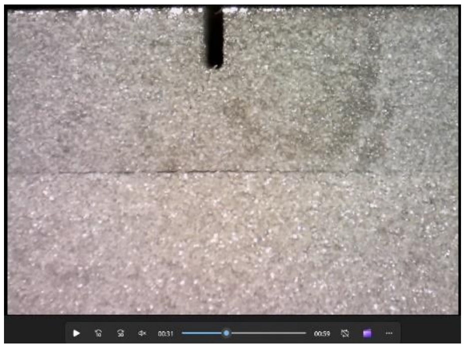

(e)

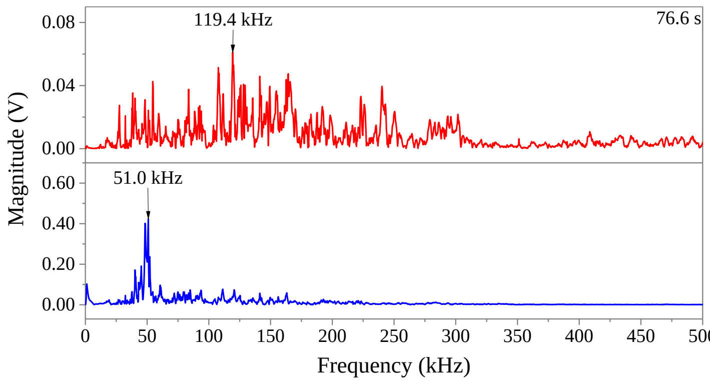
76.6 s
119.4 kHz
51.0 kHz
Magnitude (V)
Frequency (kHz)

(f)

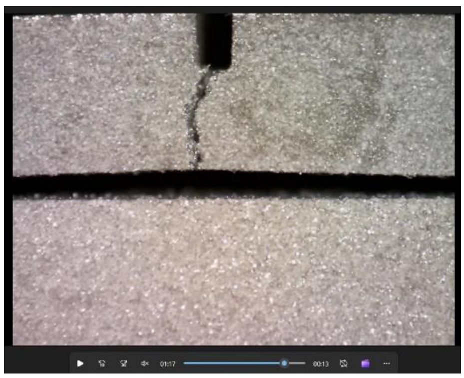

(g)

Fig.4 (a) An overlap of load-time curve with individual acoustic emission event during four-point bending test of coupon with 1mm precut. (b, d, f) Detected acoustic emission frequency by WD sensor (red) and F15a sensor (blue) at 21.7, 31.3 and 76.6 seconds, respectively, as well as (c, e, g) snapshots of the coupon from the video captured during the four-point bending at the corresponding timing of 21.7, 31.3 and 76.6 seconds.

An intermediate timing between 21.1 and 76.6 s, i.e., 31.3 s, was picked up for further analysis and verification. At 31.3 s, delamination at the interface can be seen visually while cracking can be identified under the precut, as seen in Fig. 4(e). As a result, both low (63.0 & 69.9 kHz) and high (210.6, 227.4 & 288.9 kHz) frequency events have been picked up by both sensors (Fig. 4(d)), indicating the concurrent occurrence of both cracking and delamination events.

The fractured surface can be seen in Fig. 5(a), which shows typical brittle fractured surface morphology from the CS deposit. The whole interface was not smooth but rather undulated, following the interfaces between powders which can be seen clearly from Fig. 5(b). Under high magnification, it can be seen that dominant powders have been flattened by the supersonic impact, with only two powders still having the circular top part, as highlighted in Fig. 5(b). From the fractured surface, it is evident that the Al6061 deposit fractured via interparticle instead of intergranular mode. This observation indicates that the powder boundaries are significantly weaker compared to the grain boundaries within powder itself. The 1 mm precut ensures significant maximum stress right below the tip of the precut at the center of the coupon, which outweighs other possible influencing factors such as difference in porosity, residual stress, internal cracks, etc. Therefore, only one crack beneath the precut took place. Similarly, the two coupons with R3 groove also resulted in a single crack forming below the groove. Their acoustic emission signals indicating a similar failure sequence, involving crack initiation followed by delamination and therefore were not presented here for brevity.

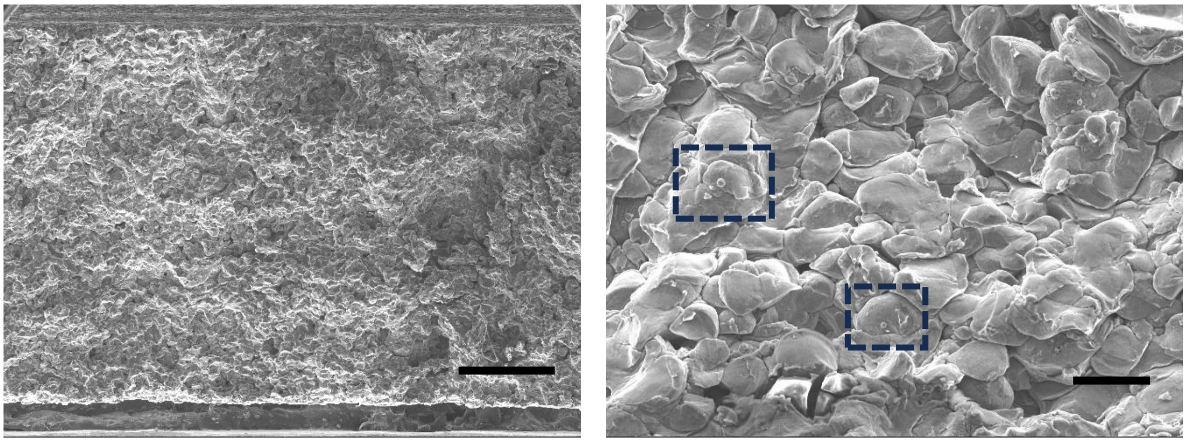

(a) (b)

Fig.5 SEM images of fractured Al6061 deposit's surface at (a) low and (b) high magnifications. Black scale bars represent 500 and 50 µm, respectively, in (a & b). The two dashed rectangular boxes in (b) highlight two Al6061 powder particles which still possess spherical top portion.

The loading-time and AE data collected from an as-prepared coupon (Fig. 2(a)) during its four-point bending test at 1.0 mm/s loading rate was also analyzed (Fig. 6(a)). The first acoustic event was detected at 43.7 s, at a load of 1995.4 N, 0.5 s ahead of the first yielding point at 44.2 s and 2001.3 N (indicated by the first green downward arrow). Due to the 66.7% higher thickness (2.5 mm) compared to that of precut sample (1.5 mm in Fig. 4), the first yielding point occurred at 70% higher load compared to that of precut sample, Fig. 4(a)). After this first yielding, the loading force decreased sharply within 2.0 s to 1779.3 N at 45.7 s, followed by a gradual decrease within 2.5 s to 1721.8 N at 48.2 s before a subsequent sharp decrease within 1.7 s to 1599.0 N at 49.9 s (indicated by the second green downward arrow). Even slowing down the play speed of the video by half (which is provided in Supplementary Information), the physical events (crack or delamination) correlated with the two yielding events cannot be identified visually. Our best conjecture is that the first yielding correlated with the initiation of a few cracks within the deposit, while the second yielding correlates with successful linkage of cracks, which thereafter propagate to the top surface and to the interface.

Despite having a thicker layer at the central plane compared to that of the precut sample, the failure sequence is the same as the precut sample. At the first AE event at 43.7 s, high frequency components of 210.6, 274.8 and 242.4 kHz were detected in both sensors (Fig. 6(b)), which correspond to the occurrence of crack and was unable to be visualized under the captured video (Fig. 6(c)). In the intermediate stage (47.8 s), a mixture of low frequencies (48.6 & 83.1 kHz) and high frequencies (300.3 kHz) were detected (Fig. 6(d)) by the sensors, which indicates the occurrence of both cracking and delamination events, which were still not visible along the sample's surface (Fig. 6(e)). At a sufficient late stage of 64.9 s, low frequency events were detected (Fig. 6(f)), where the cracks have been completed and only delamination took place (Fig. 6(g)).

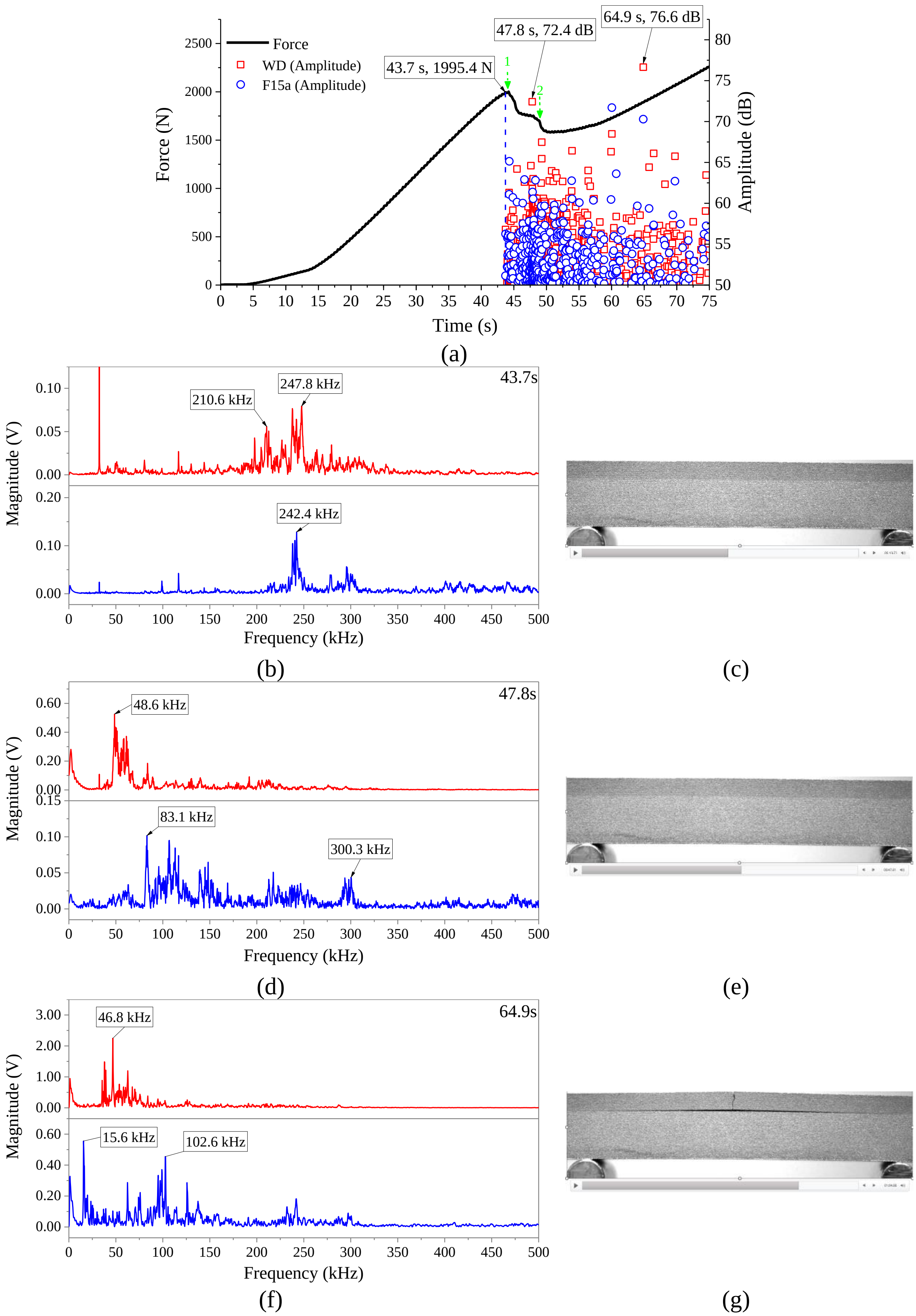
Force
WD (Amplitude)
F15a (Amplitude)
43.7 s, 1995.4 N
47.8 s, 72.4 dB
64.9 s, 76.6 dB
1
2
Force (N)
Amplitude (dB)
Time (s)
(a)
43.7s
210.6 kHz
247.8 kHz
242.4 kHz
Magnitude (V)
Frequency (kHz)
(b)
(c)
47.8s
48.6 kHz
83.1 kHz
300.3 kHz
Magnitude (V)
Frequency (kHz)
(d)
(e)
64.9s
46.8 kHz
15.6 kHz
102.6 kHz
Magnitude (V)
Frequency (kHz)
(f)
(g)

Fig. 6(a) An overlap of load-time curve with individual acoustic emission event during four-point bending of the as-prepared coupon. (b, d, f) Detected acoustic emission frequency by WD sensor (red) and F15a sensor (blue) at 43.7, 47.8 and 64.9 seconds, respectively, as well as (c, e, g) snapshots of the coupon from the video captured during the four-point bending at the corresponding timing of 43.7, 47.8 and 64.9 seconds.

Besides examining the frequencies at each discrete moment, the centroid frequencies of the AE events can also be analyzed to determine the actual failure sequence. The centroid frequency (f_c) is the frequency that corresponds to the centre of mass of the frequency distribution in the Fast Fourier Transform (FFT) spectrum. It is determined by performing an FFT on time-domain AE signals and computed with Equation 3, as seen below.

$$f_c = \frac{\sum_{i=1}^{N} A_i \cdot f_i}{\sum_{i=1}^{N} A_i} \quad (3)$$

where f_i are the frequency components in the FFT spectrum and A_i are the corresponding amplitudes of f_i [34]. For example, f_c in the 43.7, 47.8 and 64.9 s in Fig. 6 can be calculated to be 236.2, 52.9, and 44.5 kHz for WD sensor (red) and 296.6, 160.1 and 53.9 kHz for F15a sensor (blue), respectively. The centroid frequency provides useful information about the source and nature of the AE events. With the centroid frequency of AE events, different types of failure mechanisms, such as crack formation, crack growth or friction can be distinguished from one failure sequence to another.

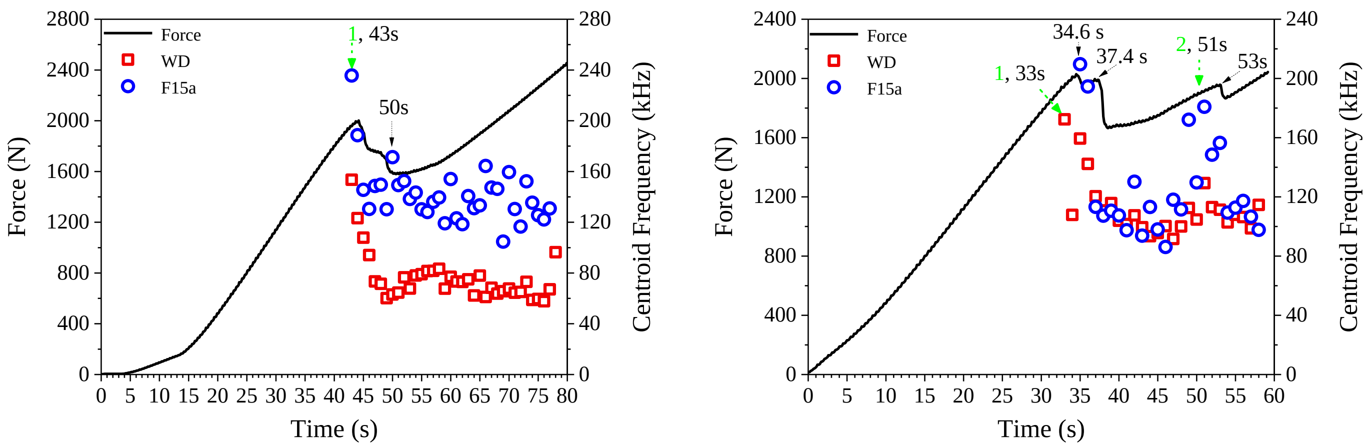

(a) (b)

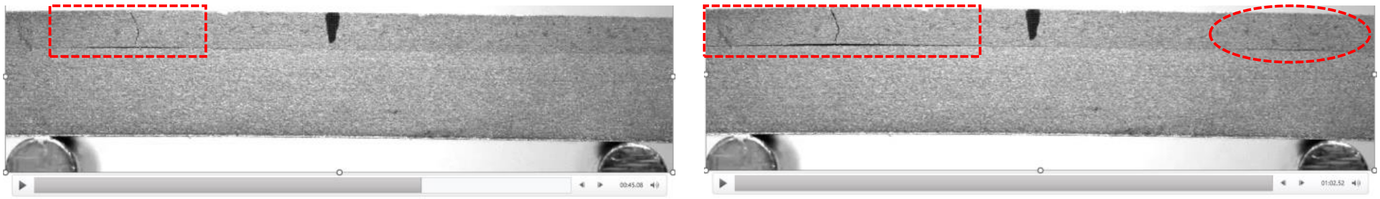

(c) (d)

Fig.7 (a) An overlap of load-time curve with cumulative centroid frequency counts of the acoustic emission detected by F15a (blue circles) and WD (red squares) sensors, respectively, for the same sample in Fig. 5. (b) Another similar plot as (a) but from the other as-prepared sample where two sequential cracks (indicated by two arrows) were detected. Images of as-prepared sample in (b) after completion of (c) the first crack at 45s marked by red dotted rectangle and (d) the second crack at 59 s marked by red dotted ellipse. The black mark is the pen ink to indicate center position.

One example can be seen in Fig. 7(a), which presents the centroid frequency from the as-prepared sample shown in Fig. 6(a). The first AE event at 43 s detected by the F15a and WD sensors had the highest centroid frequencies of 235.7 and 153.5 kHz, respectively. Similar to the discrete FFT spectrums analyzed earlier, the high centroid frequency indicates the occurrence of small scale failure mechanisms such as cracks. A second maximum centroid frequency can also be seen at 50 s at 171.2 kHz by the F15a sensor, which relates to the second yielding point in Fig. 7(a). Subsequently, the centroid frequency transitioned to a lower frequency range (~ 150 kHz and 73 kHz for F15a and WD, respectively) till the end, corresponding to the occurrence of large scale failure event (i.e., delamination) which emits low frequency AE.

Centroid frequency is not only able to detect single crack event, but it also can capture sequential cracks throughout *in-situ* loading tests. An example is the loading of second as-prepared coupon (Fig. 7(b)). The maximum centroid frequency of 172.4 kHz at 33 s corresponds to the first crack event before the first yield point at 34.6 s at a loading of 2023.3 N (marked by first green downward arrow). Similar to Fig. 7(a), there was a second yielding at 37.4 s, indicated by the connection of the cracks before they propagate through the entire 2.5

mm deposit, which can be seen at the left hand of the coupon marked in Fig. 7(c). The next maxima centroid frequencies were 180.9 and 129.3 kHz at 51 s, detected by F15a and WD sensors respectively and marked by the second downward green arrows, occurred at 2.0 s before the second yield event at 53.0 s and 1957.9 N. They indicate the second major crack event, which was also observed at the right hand of the coupon as shown in Fig. 7(d). It is worth noting that the earlier delamination at the left-hand side has laterally grown visibly.

IV. Discussion

The smallest remaining deposit thickness with 1.5 mm at the center plane for samples with a 1 mm precut and 1 mm deep groove ensured maximum stress at the center plane and hence a single crack occurred beneath the precut and groove. On the contrary, the as-prepared sample may have a single crack at the center (Fig. 6) or multiple cracks at the relative porous and weaker planes (i.e., two cracks at the two off-center near two inner pins (Fig. 7(c & d)). Despite having different number of cracks and at different locations, the three sets of Al6061 samples displayed the same failure sequence: cracks within the CS deposits form first, accompanied by delamination between the CS deposits and substrates. The results suggest that the failure sequence is dominantly determined by the nature of the deposit itself rather than sample configuration. An as-prepared sample would be simple, cost-effective yet efficient to examine failure sequence. Additional preparation of precut or groove is therefore unnecessary to save time and cost.

In the present study, we observe that cracks initially develop within the deposit, followed by delamination at the interface. This observation indicates that the failure mechanism is driven by longitudinal bending-stress, which initiates cracks in regions experiencing maximum tensile stress within the deposit. These cracks then propagate towards the coating/substrate interface, influenced by the downward bending stress. Delamination occurs subsequently at the interface due to the transverse stress. This failure mechanism aligns with classical fracture mechanics model, where the initiation of delamination is described by Westergarrd's theory [35] and further propagation of delamination is characterized by Charalambides's theory [36,37]. These insights underline the importance of analyzing both longitudinal and transverse stresses to fully understand the observed failure sequences.

It is important to clarify that the current failure sequence under four-point bending does not imply that the cohesive strength within the deposit is weaker than the adhesion strength at the interface. The observed sequence of failures is governed by the stress field generated during the four-point bending test (Fig. 8). The 2.5 mm cold-sprayed Al6061 deposit experiences a tensile stress distribution under the four-point bending test setup, as shown in Fig. 8 (a). The tensile stress is maximum at the top surface of the deposit and decreases in magnitude through the thickness down to 4.25 mm, where the central plane coincides with the neutral axis. Beyond this neutral axis, the stress transitions into compressive stress within the bottom half of the Al6061-T6 coupons. While the interface between the cold-sprayed Al6061 and Al6061-T6 substrate is also subjected to tensile stress, the magnitude of this tensile stress is significantly smaller compared to the stress at the top surface of the deposit. For the sample with 1mm precut (Fig. 8(b)) or 1mm groove, the stress distribution is similar to the one without precut in Fig. 8(a), except that the entire stress distribution profile was compressed 1mm downwards due to the presence of 1mm precut.

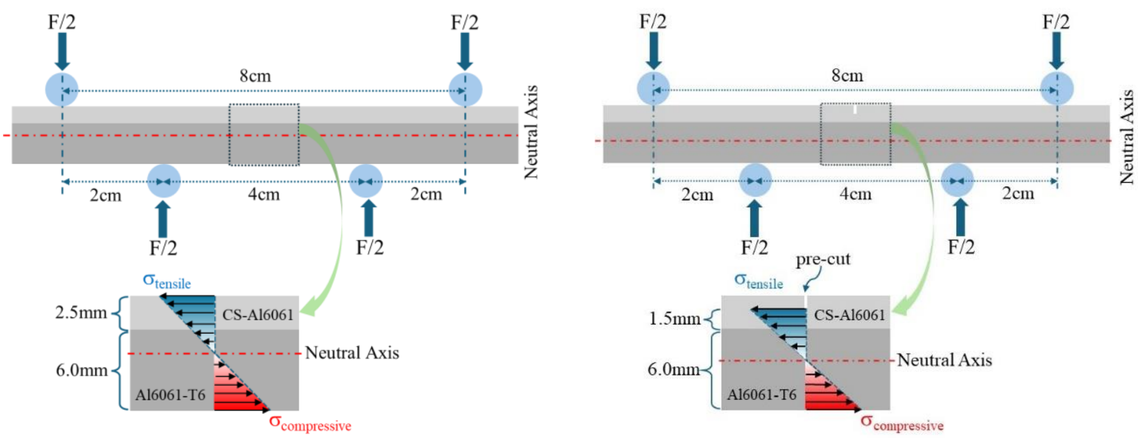

(a) (b)

Fig.8 Schematics of stress distribution during four-point bending of (a) as-prepared 2.5mm cold-sprayed (CS-) Al6061 without and (b) with a 1mm precut on 6.0 mm Al6061-T6 substrate. F represents the loading force during four-point bending.

Therefore, it would be worthwhile to investigate the influence of interfacial strength on failure sequence. One way is to prepare a relatively weaker interface without above-mentioned surface preparation like wire wheel brushing and 30° inclined deposition. Nevertheless, the interfacial strength would need be sufficiently high to withstand the delamination tendency due to the internal compressive residual stress buildup from the thick deposit. The other way is to increase inter-powder cohesive adhesion strength via post-spray heat treatment, which has been reported to enhance Al6061 deposit's ultimate tensile strength (UTS) and ductility thanks to the formation of strengthening precipitates and the localized improvement in metallurgical bonding at the particle boundaries [38].

V. Conclusion

Acoustic emission (AE) test was utilized to determine the failure sequence of 2.5 mm thick Al6061 deposit on 6.0 mm thick Al6061-T6 coupons *in-situ* during a four-point bending test, which is impractical to examine visually. Three types of sample configurations have been tested including as-prepared coupons and coupons with 1 mm precut and 1 mm deep R3 groove. The first AE event detected in all three sets of samples was at high frequency (≥ 100 kHz) which is related to crack formation between powder particles within the deposits, although the number of cracks and their appearing locations were different. After that, AE events at low frequency (< 100 kHz) which relate to delamination at the interface also took place accompanied by the propagation of the cracks towards the surface and interface. After cracks reached the interface, only low frequency AE events related to delamination were detected. Besides evaluating the frequency at each discrete moment, the centroid frequency approach can be employed to assign the failure event based on the relative magnitude of centroid frequency.

While AE sensors were used with four-point bending test in the current setup, they can certainly be integrated with other static test setup such as three-point bending and open-hole tension setup. However, additional precautions are required to filter out the background noise from the hydraulic system. With that, such AE testing can also be possibly integrated with fatigue test setups as well.

Acknowledgment

This research is supported by the Agency for Science, Technology and Research (A*STAR) under its Singapore Aerospace Program (M2115a0100 and M2415a0059) and is partially supported by the "In-Service Structural Health Monitoring (IS-SHM) for Predictive Maintenance" project funded by National Research Foundation and hosted by A*STAR under the LCER Phase 2 Programme HETFI Directed Hydrogen Programme (U2307D4002).

Data availability

The raw/processed data required to reproduce these findings cannot be shared at this time due to technical or time limitations. However, the data can be made available upon request.

Reference:

1. S. Yin, P. Cavaliere, B. Aldwell, R. Jenkins, H. Liao, W. Li, R. Lupoi, Cold spray additive manufacturing and repair: Fundamentals and applications, *Addit. Manuf.*, **21**, 628-650 (2018)
2. R.G. Maev, S. Titov, V. Leshchynsky, D. Dzhurinskiy, M. Lubrick, In situ monitoring of particle consolidation during low pressure cold spray by ultrasonic techniques, *Journal of thermal spray technology*, **20**, 845-851 (2011)
3. W. Sun, X. Chu, H. Lan, R. Huang, J. Huang, Y. Xie, J. Huang, G. Huang, Current implementation status of cold spray technology: a short review, *Journal of Thermal Spray Technology*, **31**(4), 848-865 (2022)
4. Z. Zhang, T.L. Meng, C.J.J. Lee, F. Wei, T. Ba, Z.-Q. Zhang, J. Pan, Experimental and Numerical Study of Al2219 Powders Deposition on Al2219-T6 Substrate by Cold Spray: Effects of Spray Angle, Traverse Speed, and Standoff Distance, *Materials*, **16**(15), 5240 (2023)
5. S. Msolli, Z.-Q. Zhang, D.H.L. Seng, Z. Zhang, J. Guo, C.D. Reddy, N. Sridhar, J. Pan, B.H. Tan, Q. Loi, An experimentally validated dislocation density based computational framework for

predicting microstructural evolution in cold spray process, *Int. J. Solids Struct.*, **225**, 111065 (2021)

6. D.H.L. Seng, Z. Zhang, Z.-Q. Zhang, T.L. Meng, S.L. Teo, B.H. Tan, Q. Loi, J. Pan, Influence of spray angle in cold spray deposition of Ti-6Al-4V coatings on Al6061-T6 substrates, *Surf. Coat. Technol.*, **432**, 128068 (2022)
7. Z. Zhang, D.H.L. Seng, T.L. Meng, S.L. Teo, Z.-Q. Zhang, B.H. Tan, Q. Loi, J. Pan, Effects of spray angle on mass, thickness, porosity & residual stress in cold-sprayed Ti-6Al-4V coatings, The 2nd International Conference on Advanced Surface Enhancement (INCASE 2021), 2022 (Singapore), Springer Singapore, pp 146-149
8. A. Sova, S. Grigoriev, A. Okunkova, I. Smurov, Cold spray deposition of 316L stainless steel coatings on aluminium surface with following laser post-treatment, *Surf. Coat. Technol.*, **235**, 283-289 (2013)
9. Z. Zhang, H.L.D. Seng, M. Lin, S.L. Teo, T.L. Meng, J.J.C. Lee, Z.-Q. Zhang, T. Ba, J. Guo, K. Sundaravadivelu, P.K. Aw, J. Pan, Cold spray deposition of Inconel 718 in comparison with atmospheric plasma spray deposition, *Appl. Surf. Sci.*, **535**, 147704 (2021)
10. D.H.L. Seng, Z. Zhang, Z.-Q. Zhang, T.L. Meng, S.L. Teo, B.H. Tan, Q. Loi, J. Pan, T. Ba, Impact of spray angle and particle velocity in cold sprayed IN718 coatings, *Surf. Coat. Technol.*, **466**, 129623 (2023)
11. H. Assadi, H. Kreye, F. Gärtner, T. Klassen, Cold spraying – A materials perspective, *Acta Mater.*, **116**, 382-407 (2016)
12. P. Cavaliere, A. Silvello, Crack repair in aerospace aluminum alloy panels by cold spray, *J. Therm. Spray Technol.*, **26**(4), 661-670 (2017)
13. D. Greving, How Cold Spray is Changing Aerospace Aftermarket Repair Strategies, North American Cold Spray Conference, 2016 (Edmonton, Alberta, Canada)
14. D. Soboń, Application of cold sprayed coatings in aviation and automotive, 2018 XI International Science-Technical Conference Automotive Safety, 18-20 April, 2018
15. S. Krebs, F. Gärtner, T. Klassen, Cold Spraying of Cu-Al-Bronze for Cavitation Protection in Marine Environments, *J. Therm. Spray Technol.*, **24**(1-2), 126-135 (2015)
16. G. Mathers, The Welding of Aluminium and its Alloys, Woodhead Publishing, 2002
17. K. Petráčková, J. Kondás, M. Guagliano, Fixing a hole (with cold spray), *Int. J. Fatigue*, **110**, 144-152 (2018)
18. B. White, W. Story, L. Brewer, J.B. Jordon, Fatigue behaviour of fastener holes in high-strength aluminium plates repaired by cold spray deposition, *Fatigue Fract. Eng. Mater. Struct.*, **43**(2), 317-329 (2020)
19. M. Yandouzi, S. Gaydos, D. Guo, R. Ghelichi, B. Jodoin, Aircraft Skin Restoration and Evaluation, *J. Therm. Spray Technol.*, **23**(8), 1281-1290 (2014)
20. Acoustic Emission Testing, Nondestructive Testing Handbooked., R.K. Miller, E.K. Hill, P.O. Moore, Eds., American Society for Nondestructive Testing (ASNT), 2005
21. V. Viswanathan, A. Prathuru, N.H. Faisal, S. Goel, Acoustic Emission Sensor-Assisted Process Monitoring of Air Plasma-Sprayed Titanium Deposition, *Journal of Thermal Spray Technology*, **32**(8), 2763-2777 (2023)
22. W. Tillmann, F. Walther, W. Luo, M. Haack, J. Nellesen, M. Knyazeva, In situ acoustic monitoring of thermal spray process using high-frequency impulse measurements, *Journal of Thermal Spray Technology*, **27**, 50-58 (2018)
23. P.R. Prem, A.R. Murthy, Acoustic emission monitoring of reinforced concrete beams subjected to four-point-bending, *Applied Acoustics*, **117**, 28-38 (2017)
24. J.-n. Jing, L.-h. Dong, H.-d. Wang, G. Jin, Application of acoustic emission technology for quantitative characterization of plasma-sprayed coatings subjected to bending fatigue tests, *Journal of Thermal Spray Technology*, **27**, 1090-1102 (2018)
25. K.M. Holford, M.J. Eaton, J.J. Hensman, R. Pullin, S.L. Evans, N. Dervilis, K. Worden, A new methodology for automating acoustic emission detection of metallic fatigue fractures in

highly demanding aerospace environments: An overview, *Progress in Aerospace Sciences*, **90**, 1-11 (2017)

26. S. Grigg, C.A. Featherston, M. Pearson, R. Pullin, Advanced Acoustic Emission Source Location in Aircraft Structural Testing, *IOP Conf. Ser.: Mater. Sci. Eng.*, **1024**(1), 012029 (2021)
27. C. Tuloup, W. Harizi, Z. Aboura, Y. Meyer, Structural health monitoring of polymer-matrix composite using embedded piezoelectric ceramic transducers during several four-points bending tests, *Smart Materials and Structures*, **29**(12), 125011 (2020)
28. Acoustic Emission Testing: Basics for Research – Applications in Engineering, M.O. Christian U. Grosse, Dimitrios G. Aggelis, Tomoki Shiotani, Ed., Springer Cham, 2021
29. Z.N. Valentyn Skalskyi, Olena Stankevych, Acoustic Emission: Fracture Detection in Structural Materials, Springer Cham, 2022
30. P.L. Clavette, M.A. Klecka, A.T. Nardi, G.C. Ojard, R.S. Gostautas, Real time NDE of cold spray processing using acoustic emission, The 33rd IMAC, A Conference and Exposition on Structural Dynamics, C. Niezrecki Ed., 2015 (Cham), Springer International Publishing, pp 27-36
31. Acoustic Emission Testing: Basics for Research – Applications in Engineering, M.O. Christian U. Grosse, Dimitrios G. Aggelis, Tomoki Shiotani, Ed., Springer Cham, 2022
32. L. Wang, C. Ming, X.H. Zhong, J.X. Ni, S.Y. Tao, F.F. Zhou, Y. Wang, Prediction of critical rupture of plasma-sprayed yttria stabilized zirconia thermal barrier coatings under burner rig test via finite element simulation and in-situ acoustic emission technique, *Surface and Coatings Technology*, **367**, 58-74 (2019)
33. W.B. Yao, C.Y. Dai, W.G. Mao, C. Lu, L. Yang, Y.C. Zhou, Acoustic emission analysis on tensile failure of air plasma-sprayed thermal barrier coatings, *Surface and Coatings Technology*, **206**(18), 3803-3807 (2012)
34. E. Maillet, C. Baker, G.N. Morscher, V.V. Pujar, J.R. Lemanski, Feasibility and limitations of damage identification in composite materials using acoustic emission, *Composites Part A: Applied Science and Manufacturing*, **75**, 77-83 (2015)
35. H.M. Westergaard, Bearing Pressures and Cracks: Bearing Pressures Through a Slightly Waved Surface or Through a Nearly Flat Part of a Cylinder, and Related Problems of Cracks, *Journal of Applied Mechanics*, **6**(2), A49-A53 (1939)
36. P.G. Charalambides, R.M. Mcmeeking, Near-Tip Mechanics of Stress-Induced Microcracking in Brittle Materials, *J. Am. Ceram. Soc.*, **71**(6), 465-472 (1988)
37. P.G. Charalambides, H.C. Cao, J. Lund, A.G. Evans, Development of a test method for measuring the mixed mode fracture resistance of bimaterial interfaces, *Mechanics of Materials*, **8**(4), 269-283 (1990)
38. M.R. Rokni, C.A. Widener, O.C. Ozdemir, G.A. Crawford, Microstructure and mechanical properties of cold sprayed 6061 Al in as-sprayed and heat treated condition, *Surf. Coat. Technol.*, **309**, 641-650 (2017)